

Wind flow measurement over the Subaru Telescope

**Hirofumi Horikawa^{1*}, Naoshi Baba¹, Masashi Ohtsubo², Yuji Norimoto³,
Tetsuo Nishimura⁴, and Noriaki Miura⁵**

¹Department of Applied Physics, Hokkaido University, Sapporo 060-8628, Japan, ²National
Astronomical Observatory of Japan, Mitaka 181-8588, Japan, ³Okayama Astrophysical
Observatory, NAOJ, Kamogata 719-0232, Japan, ⁴Subaru Telescope, NAOJ, Hilo, HI 96720,
USA, ⁵Department of Computer Sciences, Kitami Institute of Technology, Kitami 090-8507,
Japan

Wind flows over the Subaru 8.2m telescope on Mauna Kea in Hawaii are analyzed with a correlation method. Three or four wind flows were detected from our measurement. Spatial and temporal resolutions of the wind flow analysis across the 8.2m pupil are investigated experimentally. A 3-D spatiotemporal-frequency analysis is also applied to the wind-flow data.

c2003 Optical Society of America

OCIS codes: 010.1330, 110.6770, 030.6140, 120.6150, 100.2000

*) Now with the System R&D Department, Ricoh Co., Ltd., Yokohama 224-0035, Japan.

1. Introduction

Wind measurements at and above astronomical sites have been widely conducted because astronomical seeing is strongly related to wind flows and their layered structure¹. One of the methods of wind flow analysis is to take correlation of atmospheric speckle patterns (stellar scintillation patterns) across the telescope pupil²⁻⁶. The speckle patterns are produced on a detection plane by diffraction at the atmospheric turbulent layers. To measure wind flows over the Subaru 8.2m telescope on Mauna Kea, Hawaii, the Visible Test Observation System (VTOS) has been developed as one of the Cassegrain focus test instruments prepared to study the characteristics of the Subaru Telescope in the visible wavelengths.

In previous reports³⁻⁶, single-element detectors such as photomultipliers have been used together with two-dimensional detectors. VTOS uses only two-dimensional detector, an image-intensified CCD (ICCD) camera, to detect speckle patterns over the pupil. For cross-correlation of speckle patterns, the two-dimensional image frames are used for the detection of the wind flows across the entire pupil plane of the 8.2m Subaru Telescope. The pupil image is divided into a few sub-pupils and the speckle patterns in each of the sub-pupil are used. From this analysis, we estimate the size of the sub-pupil needed to detect wind flows. Next, the video frames are temporally grouped and we estimate the number of video frames to detect wind flows. This gives temporal resolution of the wind flow analysis.

Vernin and Roddier⁸ analyzed 2-D spatiotemporal power spectra of stellar light scintillation. In our paper, a 3-D spatiotemporal-frequency analysis of the speckle patterns, analogous to the optical flow analysis^{9,10}, is conducted. A set of the video frames is Fourier-transformed in three dimensions. This 3-D spatiotemporal-frequency analysis shows the existence of steady wind flows and confirms Taylor hypothesis¹ that a wind, uniform throughout

the turbulence, merely drives the wave-front perturbations without deformation over the telescope pupil plane. Caccia *et al.*⁴ verified Taylor's hypothesis for one particular layer from their spatiotemporal cross-correlation analysis. Our 3-D spatiotemporal frequency analysis is able to test Taylor's hypothesis for multiple layers at a time.

2. Observation

VTOS was attached to the Cassegrain focus of the Subaru Telescope by using the CIAX (Cassegrain Instrument Automatic eXchanger) system⁷ that swaps three small instruments mounted on the telescope Cassegrain focus. VTOS is designed to analyze image motion on the Cassegrain focal plane, to conduct phase-diversity imaging for telescope mirror analysis¹¹, and to observe stellar speckle and speckle-spectroscopic interferograms¹². A camera lens with a focal length of 50 mm is used to image the pupil of the telescope. The ICCD camera used to detect speckle patterns runs at the video frame rate, 30 frames/sec.

The observation was conducted on June 11, 1999. A star (HD207469) with the visual magnitude 6.8 was observed. The elevation angle of the telescope during the observation was 65~70 degrees. No interference filter was used and the bandwidth was limited by the spectral response of the ICCD camera from 450 to 820 nm. One of the data frames is shown in Fig. 1. The image of the entire primary mirror is shown and the speckle patterns caused by the stellar scintillation inside the pupil boundary can be seen. One frame consists of 640x480 pixels and the pupil image is included within 320x320-pixel region in Fig. 1. One pixel size corresponds to 2.56 cm on the primary mirror. Consecutive 512 video frames are stored in the PC memory and form one data set. The duration of a data set is, therefore, $512/30=17.1$ seconds for the video frame rate.

3. Data preprocessing

Each video frame is divided into even and odd interlaced fields. Each field then consists of 320x480 pixels and the effective frame rate of the field-data is 60 frames/sec. Taking running average of two adjacent pixels along the row makes each field 320x240 pixels. In this format the diameter of the pupil image is 160 pixels and one pixel size corresponds to 5.13 cm on the primary mirror. Two data sets of 512 each for even- and odd-fields are formed from one data set of 512 video frames.

A long exposure image or an average of the field-data through an observation session is necessary to estimate an offset component. The offset of the data used in the following analysis is subtracted by:

$$f_i(x, y, t) = \hat{f}_i(x, y, t) - \langle \hat{f}_i(x, y, t) \rangle_t, \quad i=odd \text{ or } even, \quad (1)$$

where $\hat{f}_i(x, y, t)$ is a field-data taken with the ICCD camera and $\langle \rangle_t$ represents the time average through the session. For example, Fig. 2(a) shows an effective long exposure image of the telescope pupil and Fig. 2(b) is one frame of the field-data with the offset removed by the Eq. (1).

4. Correlation analysis

To detect the movement of the speckle patterns, the degree of cross-correlation is calculated as

$$\rho_\tau(\xi, \eta) = \frac{\tau}{T} \sum_{t=\tau}^T \frac{\sum_{x,y}^S f(x, y, t) \times f(x - \xi, y - \eta, t - \tau)}{\sqrt{\left(\sum_{x,y}^S |f(x, y, t)|^2 \right) \times \left(\sum_{x,y}^S |f(x - \xi, y - \eta, t - \tau)|^2 \right)}}, \quad (2)$$

where τ is the time interval between two field-data, T , the duration of an observation session, S , the overlapping area of the shifted pupil-images, and (ξ, η) , the amount of the shift. The shadow areas of the secondary support spider and the secondary mirror are excluded from S .

Figures 3(a) and (b) show the results of cross-correlation from the data at 13:28 and 13:32 (UT) on June 11, 1999, respectively. In the calculation, 512 odd- and even-field data were used separately and the two cross-correlation results were combined. In the cross-correlation the time interval τ should be chosen appropriately. For this analysis τ was set to 0.1 sec to detect wind flows with ~ 10 m/sec. When there are faster wind components, τ shorter than 0.1 sec should be used. Three and four peaks are found in Figs. 3(a) and (b), respectively. This agrees with the general view that atmospheric turbulence profiles are characterized by a small number of thin strong turbulence layers superposed on a weaker background of distributed turbulences.¹³ It is known that the easterly trade winds and the prevailing westerlies blow throughout the year over the Hawaii Island. It looks that the detected 8.7 m/sec wind corresponds to the westerly, and the 4.4 m/sec wind in Fig. 3(a) and the 3.0 m/sec component in Fig. 3(b) correspond to the trade winds. These two components persist in the results from two other data sets, which were taken several-tens minutes later. The accuracy of the wind speed is ± 0.3 m/sec in our measurement. Wind flows faster than 10 m/s were not found, even when τ was set to less than 0.1 sec.

To investigate how fast winds change, we vary the number of the data frames in the intervals that correlation is calculated. In the calculation above, 512 data frames were used and its total data acquisition time was 17.1 seconds. Figure 4 shows the cross-correlation results versus the data-frame acquisition time T , where τ is fixed to 0.1 sec. The results for the data at 13:28 and at 13:32 are shown in Figs. 4(a) and (b), respectively. As can be seen, the correlation

peaks appear clearly around $T=1.67$ sec. Therefore, a set of the video data with $T=2$ sec is considered to be enough to calculate the cross-correlation given in Eq. (2). The temporal change of winds, therefore, can be detected with a resolution of about 2 seconds.

Next, we divide the pupil image into 2x2, 3x3, 4x4 and 5x5 areas and calculate the cross-correlation on each divided area. Figures 5(a)-(d) show the results of the cross-correlations for the data set of the 512 frames at 13:28. From these figures the correlation peaks become unclear toward the case of 5x5 divisions. A detectability of correlation peaks was assessed by standard deviation σ of the correlation map. The smallest peak should be greater than 2σ . Since the diameter of the effective aperture is 8.2 m, the region needed to detect wind flows would be around $1.5 \times 1.5 \text{ m}^2$, which is the spatial resolution for our wind flow analysis.

5. Spatiotemporal-frequency analysis

Movement of an object without changing shape is analyzed with 3-D spatiotemporal Fourier method, which has been applied to optical flow analysis^{9,10}. This method can be used to detect speckle patterns within the pupil image that move without changing their shapes. Suppose that the image data consist of superposition of unchanging patterns with a constant velocity V_j ;

$$\begin{aligned}
 f(x, y, t) &= \sum_j g_j(x, y, t) \\
 &= \sum_j g_j(x - V_{jx}t, y - V_{jy}t). \tag{3}
 \end{aligned}$$

The 3-D Fourier transform of $f(x, y, t)$ becomes

$$\begin{aligned}
F(u, v, \nu) &= \iiint f(x, y, t) \exp\{-i2\pi(ux + vy + \nu t)\} dx dy dt \\
&= \iiint \sum_j g_j(x - V_{jx}t, y - V_{jy}t) \exp\{-i2\pi(ux + vy + \nu t)\} dx dy dt .
\end{aligned} \tag{4}$$

Substitution of new variables

$$X_j = x - V_{jx}t, \quad Y_j = y - V_{jy}t \tag{5}$$

into Eq. (4) leads to

$$\begin{aligned}
F(u, v, \nu) &= \sum_j \left[\iint g_j(X_j, Y_j) \exp\{-i2\pi(uX_j + vY_j)\} dX_j dY_j \int \exp\{-i2\pi(uV_{jx} + vV_{jy} + \nu)t\} dt \right] \\
&= \sum_j G_j(u, v) \times \delta(uV_{jx} + vV_{jy} + \nu) ,
\end{aligned} \tag{6}$$

where $G_j(u, v)$ is 2-D spatial Fourier transform of $g_j(X_j, Y_j)$. From Eq. (6) $F(u, v, \nu)$ becomes nonzero only on the planes

$$uV_{jx} + vV_{jy} + \nu = 0 . \tag{7}$$

The planes of Eq. (7) pass through the origin of the 3-D frequency space. The normal vectors to the planes are $(1/V_{jx}, 1/V_{jy}, 1)$ and depend on the velocities of the moving patterns. Figure 6 shows schematically the relationship between the 3-D data cube of $f(x, y, t)$ and its 3-D Fourier spectra of $F(u, v, \nu)$.

Figures 7(a) and (b) show the cross-sections of the 3-D power spectra at $\nu=3$ Hz and $\nu=6$ Hz, respectively, for the data set of the 512 frames at 13:28 (UT). For comparison, the broken lines in Figs. 8(a) and (b) are the expected lines from the results of Fig. 3 at $\nu=3$ Hz and $\nu=6$ Hz, respectively. The numbering in Fig. 8 is the same as in Fig. 3. The appearance of several lines indicate that there are several kinds of fixed patterns that move with different constant velocities and in different directions in the sequence of the data frames. Such a phenomenon can be interpreted with Taylor hypothesis of atmospheric turbulence. It should be noted that the result in Fig. 3 is derived from the cross-correlation between data frames separated by 0.1 seconds. For the 3-D Fourier transformation, on the other hand, all the 512 data frames are simultaneously used.

When the 3-D power spectra are localized on several planes, $|G_j(u, \nu)|^2$ can be extracted. The inverse Fourier transformation of $|G_j(u, \nu)|^2$ gives the auto-correlation of the j -th speckle patterns. As pointed out by Cassia *et al.*⁴ the shape of the correlation peak can be used to evaluate the height of the j -th turbulent layer because speckle sizes depend on the propagation path distances from the turbulent layer to the detection plane. We extracted three planes from the 3-D power spectra as shown in Fig. 7 and calculated the three auto-correlations. However, no significant differences were seen in the shapes of the three auto-correlations. This is mainly because the magnification of our detection system is not large enough to discriminate the different sizes of the speckle patterns.

6. Conclusion

An ICCD camera was used to detect wind flows across the pupil of the Subaru Telescope in Hawaii. The temporal resolution required to find the correlation peaks resulted from wind flows is estimated to be around 2 seconds in our method. The temporal change of wind flows will be measured with such a temporal resolution. By dividing the pupil image and calculating the correlation of the speckle patterns it was found that sub-pupils of the size $\sim 1.5 \times 1.5 \text{ m}^2$ are necessary to detect wind flows. This means that local wind flows over the primary mirror can be investigated with such a spatial resolution.

The 3-D spatiotemporal-frequency analysis reveals several components of constant flows with nearly unchanging patterns. This confirms Taylor's frozen flow hypothesis by using the 8.2 m pupil's data. It will be interesting and observationally useful to examine the relationship between the seeing and the wind flows over the Subaru Telescope.

We acknowledge A. Miyashita and N. Takato of the National Astronomical Observatory of Japan for helpful discussions on the winds over the Subaru Telescope.

References

1. F. Roddier, "The effect of atmospheric turbulence in optical astronomy," in *Progress in Optics XIX*, E. Wolf, ed. (North-Holland, Amsterdam, 1981), pp. 281-376.
2. A. Rocca, F. Roddier, and J. Vernin, "Detection of atmospheric turbulent layers by spatiotemporal and spatioangular correlation measurements of stellar-light scintillation," *J. Opt. Soc. Am.* **64**, 1000-1004 (1974).
3. M. Azouit and J. Vernin, "Remote investigation of tropospheric turbulence by two-dimensional analysis of stellar scintillation," *J. Atmos. Sci.* **37**, 1550-1557 (1980).
4. J.L. Caccia, M. Azouit, and J. Vernin, "Wind and C_N^2 profiling by single-star scintillation analysis," *Appl. Opt.* **26**, 1288-1294 (1987).
5. R. Li, M. Takabe, and T. Aruga, "A new data acquisition system for measuring the movement of atmospheric speckle patterns," *Rev. Sci. Instrum.* **70**, 2136-2139 (1999).
6. S. Oya, M. Takabe, and T. Aruga, "Application of an exclusively binarized correlation-calculation method to wind velocity measurement by use of stellar scintillation patterns," *Appl. Opt.* **40**, 4041-4049 (2001).
7. T. Usuda, K. Omata, M. Yutani, Y. Torii, Y. Mikami, T. Nishino, T. Noguchi, T. Nishimura, S. Sawada, and the Subaru Project team, "CIAX: Cassegrain Instrument Auto eXchanger for the Subaru Telescope," *Proc. SPIE* **4009**, 141-150 (2000).
8. J. Vernin and F. Roddier, "Experimental determination of two-dimensional spatiotemporal power spectra of stellar light scintillation. Evidence for a multiplayer structure of the air turbulence in the upper troposphere," *J. Opt. Soc. Am.* **63**, 270-273 (1973).
9. A. B. Watson and A. J. Ahumada, Jr., "Model of human visual-motion sensing," *J. Opt. Soc. Am.* **A2**, 322-342 (1985).

10. D. J. Heeger, "Model for the extraction of image flow," J. Opt. Soc. Am. **A4**, 1455-1471 (1987).
11. N. Baba and K. Mutoh, "Measurement of telescope aberrations through atmospheric turbulence by use of phase diversity," Appl. Opt. **40**, 544-552 (2001).
12. N. Baba, S. Kuwamura, and Y. Norimoto, "Stellar speckle camera for spectroscopy," Appl. Opt. **33**, 6662-6666 (1994).
13. R. C. Flicker and F. J. Rigaut, "Hokupa'a anisoplanatism and Mauna Kea turbulence characterization," Publ. Astron. Soc. Pacific **114**, 1006-1015 (2002).

Figure Captions

Fig. 1 A video frame of the pupil of the Subaru 8.2 m telescope. The pupil is imaged in the 320x320 pixel region. Speckle patterns caused by atmospheric turbulence are seen inside the pupil image.

Fig. 2 (a) An effective long exposure image of the pupil, which constitutes the bias component of the field-data. (b) One of the field-data for the analysis, where the bias component is subtracted.

Fig. 3 Degree of cross-correlation displayed in gray-scale map (left) and contour plot (right). The arrows in the contour map are drawn from the origin to the local peaks of the cross-correlation. (a) Data at 13:28 and (b) at 13:32 on June 11, 1999 (UT).

Fig. 4 A gray-scale map of the degree of cross-correlation vs. data-frame acquisition time. For the data at (a) 13:28 and (b) 13:32 on June 11, 1999 (UT).

Fig. 5 The degree of cross-correlation calculated for the divided pupil image; (a) 2x2, (b) 3x3, (c) 4x4, and (d) 5x5 divisions. The result for the entire pupil is shown in Fig. 3(a).

Fig. 6 The 3-D data cube and its Fourier spectra. When fixed patterns move with a constant velocity, their spatiotemporal-frequency spectra localize on a plane that passes through the origin.

Fig. 7 The cross-sections of the 3-D power spectra at (a) $\nu=3$ Hz and (b) $\nu=6$ Hz, respectively. These figures indicate that the spectra are localized mostly on three planes.

Fig. 8 Expected lines from the result of Fig. 4(a) on the cross-sections of the 3-D power spectra at (a) $\nu=3$ Hz and (b) $\nu=6$ Hz, respectively. These lines match to those in Fig. 7.

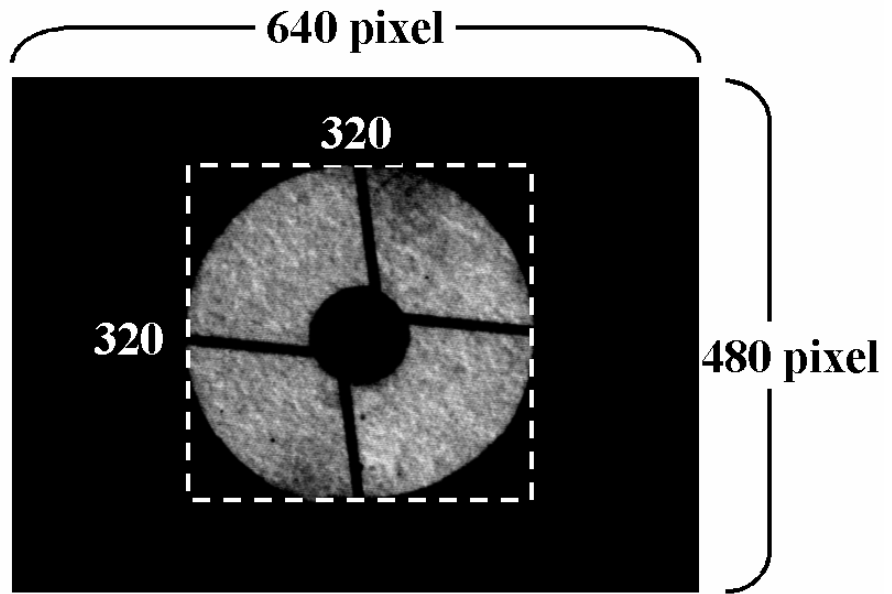
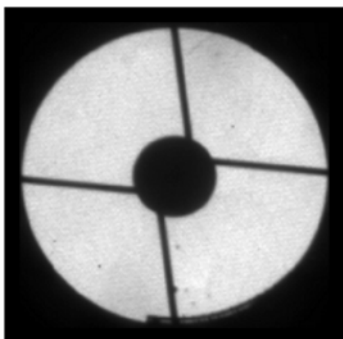
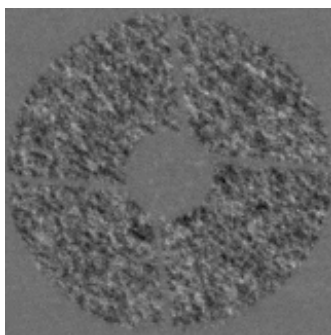


Fig. 1

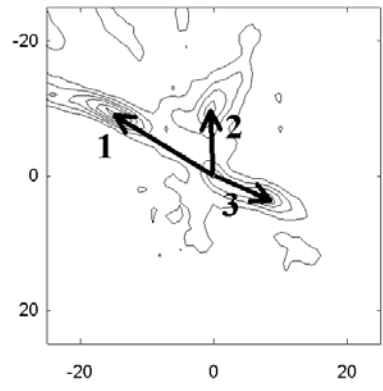
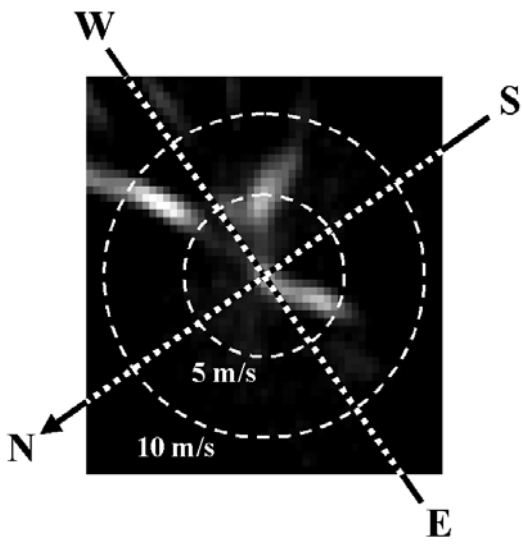


(a)



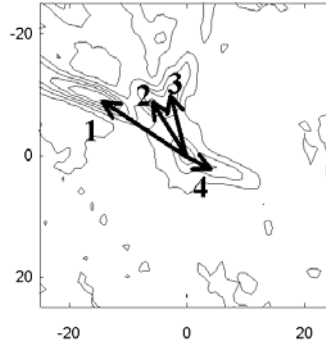
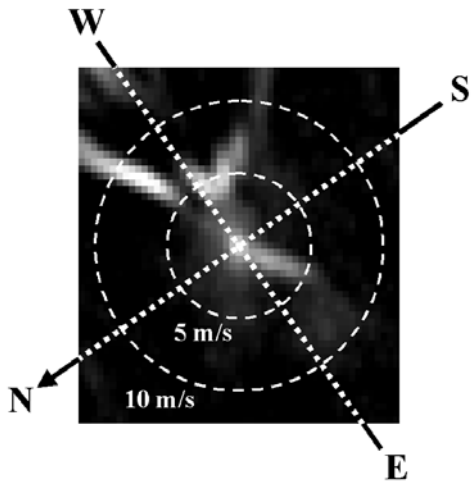
(b)

Fig. 2



- 1: 8.7 m/s**
- 2: 4.9 m/s**
- 3: 4.4 m/s**

Fig. 3 (a)



- 1: 8.7 m/s**
- 2: 5.8 m/s**
- 3: 5.1 m/s**
- 4: 3.0 m/s**

Fig.3(b)

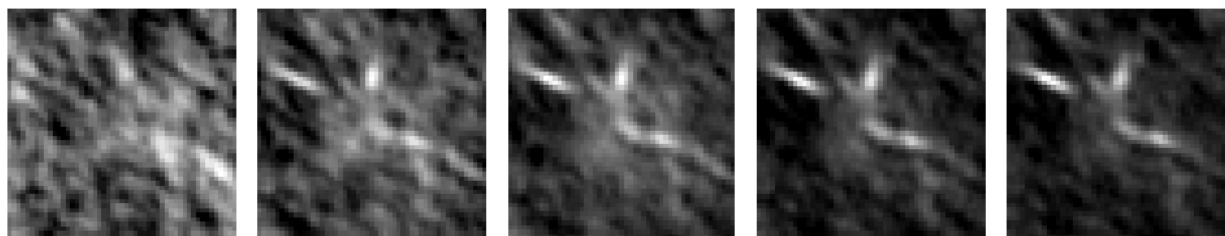
$T=0.33$ sec

0.67 sec

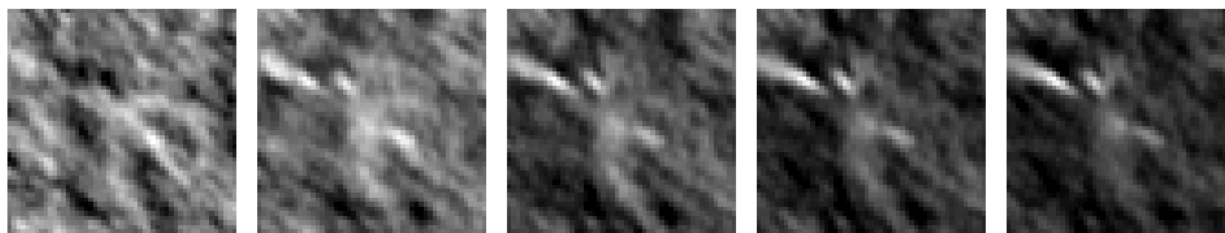
1.00 sec

1.33 sec

1.67 sec



(a)



(b)

Fig. 4

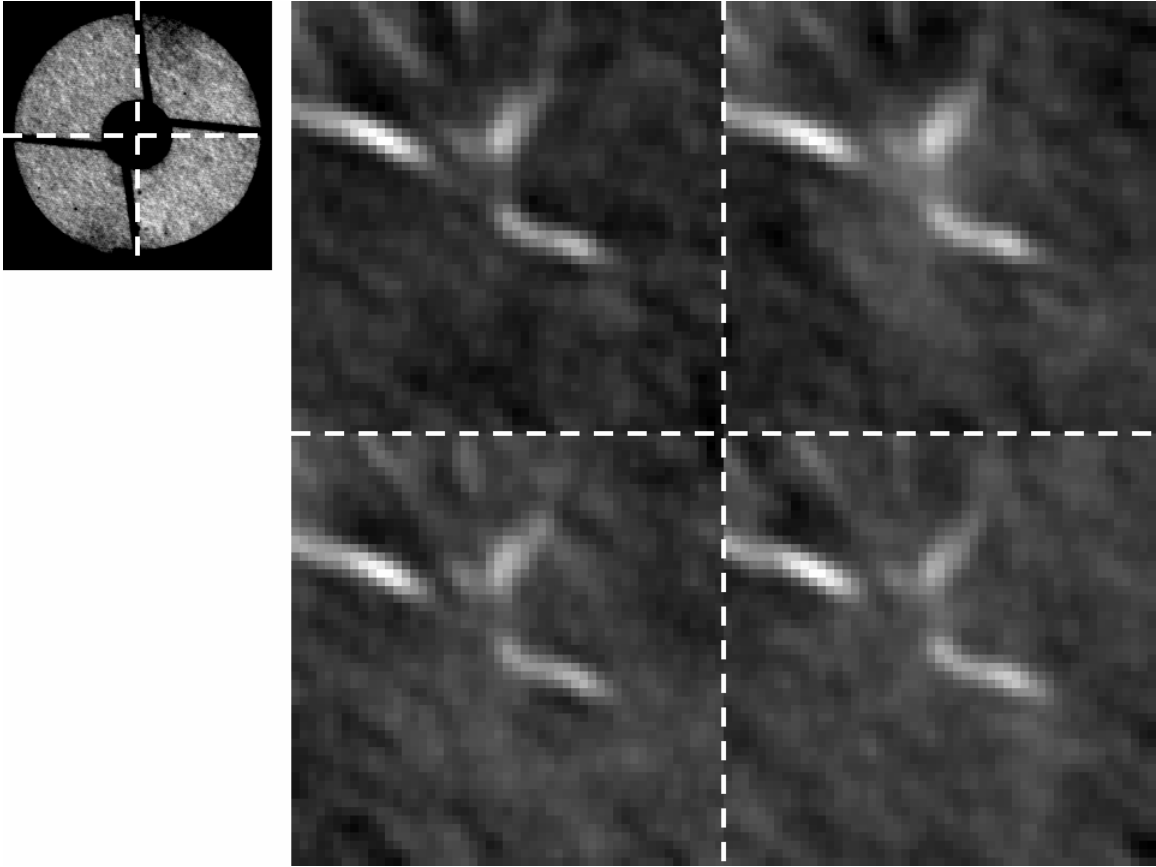


Fig. 5 (a)

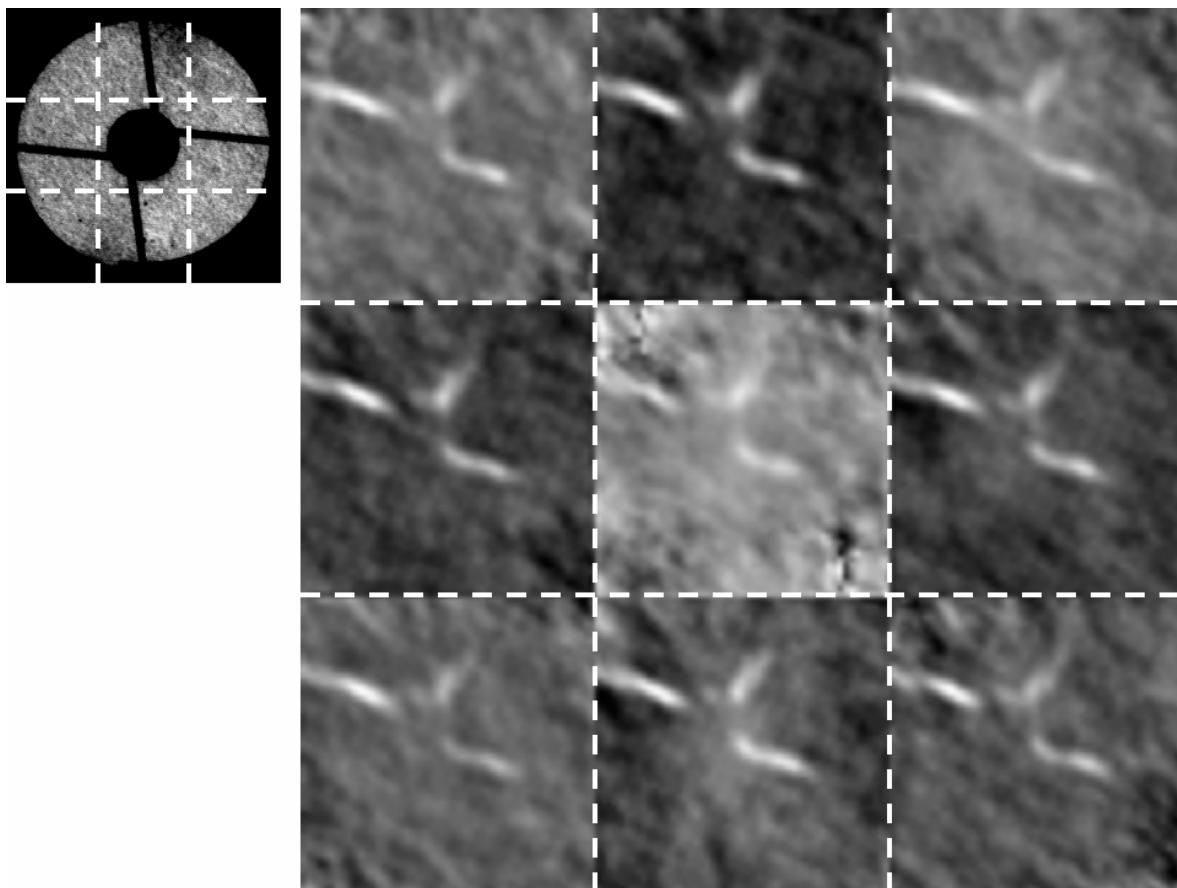


Fig. 5 (b)

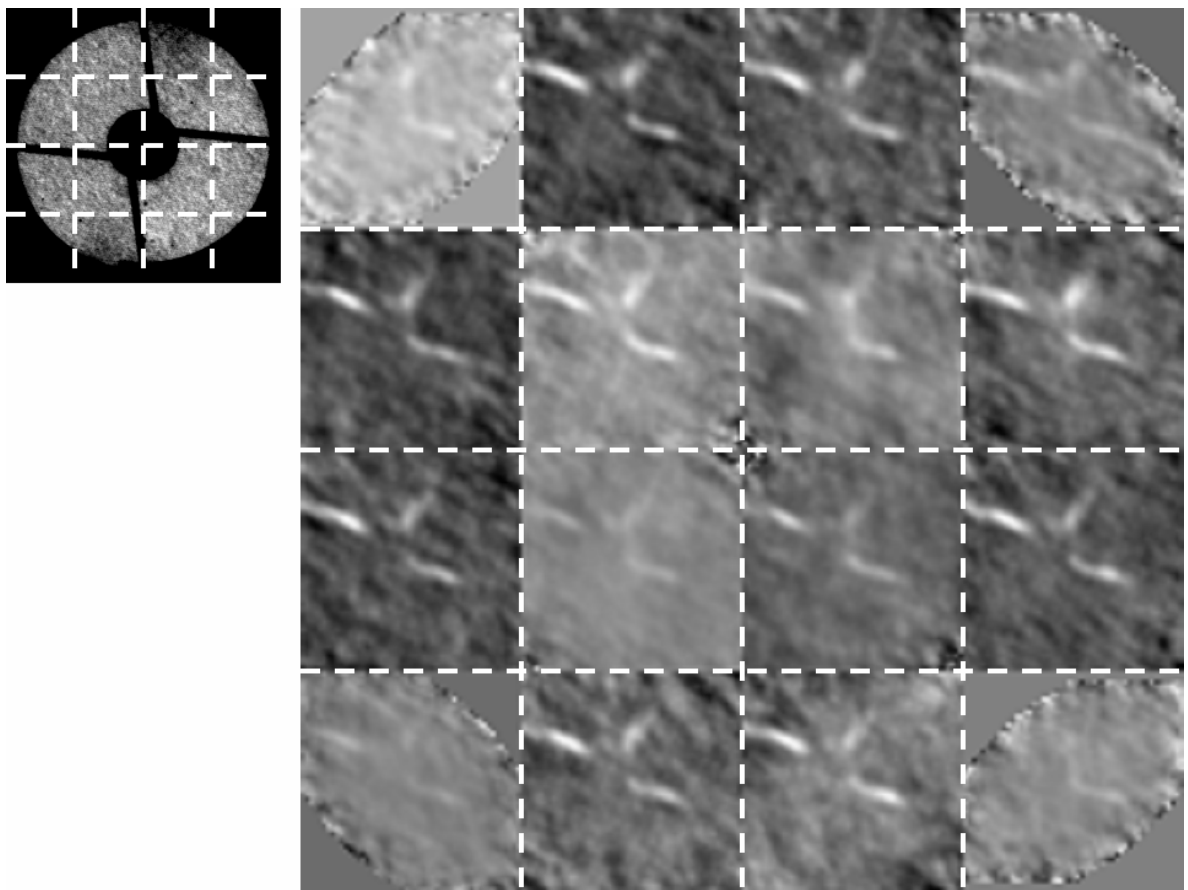


Fig. 5 (c)

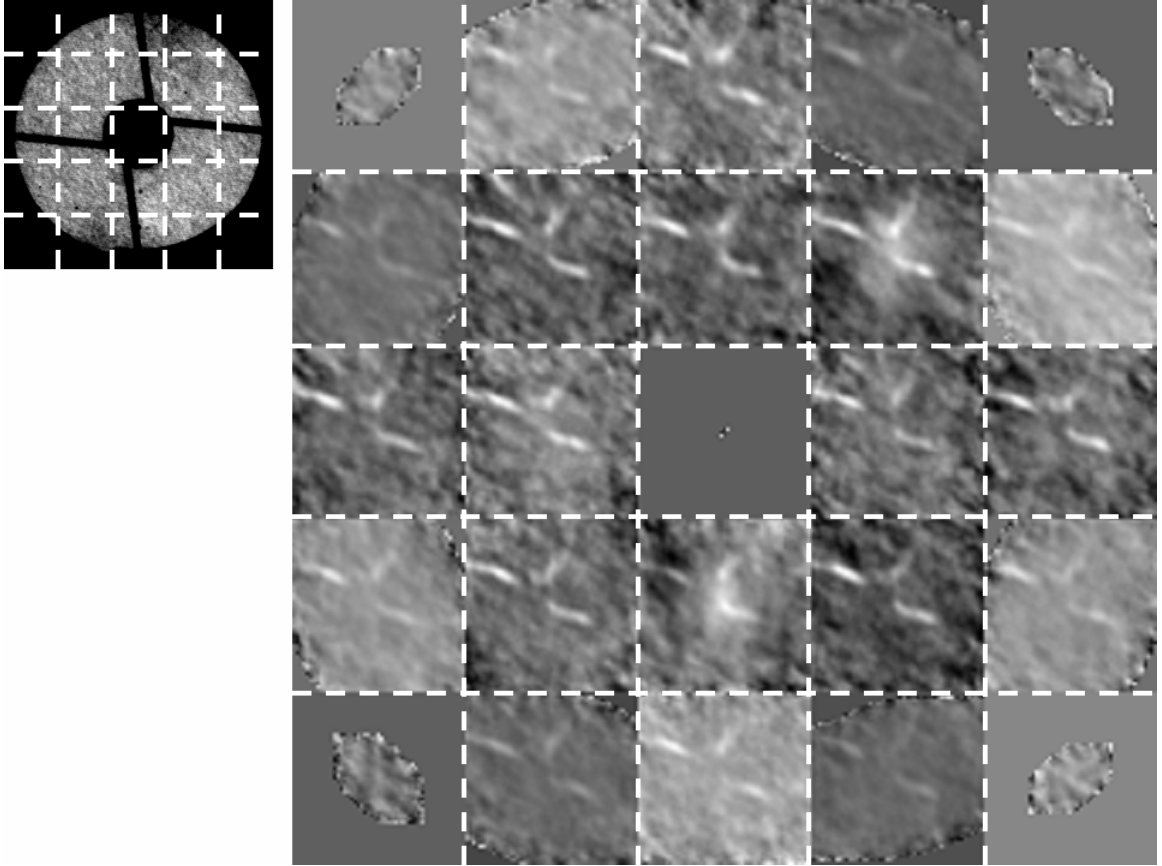


Fig. 5 (d)

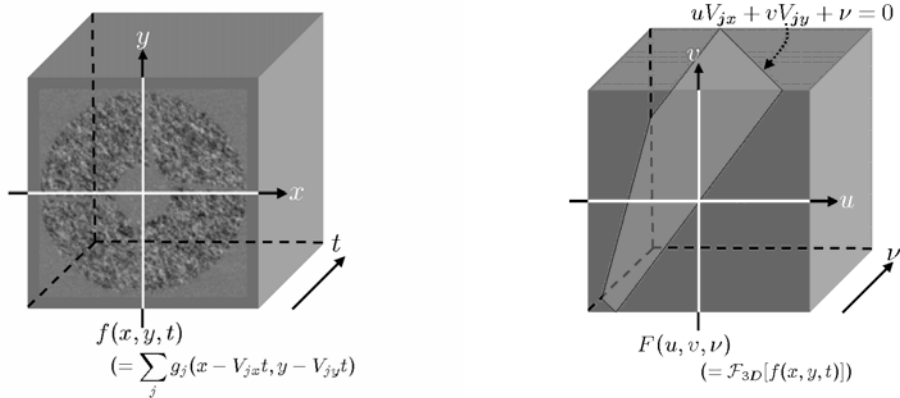


Fig.6

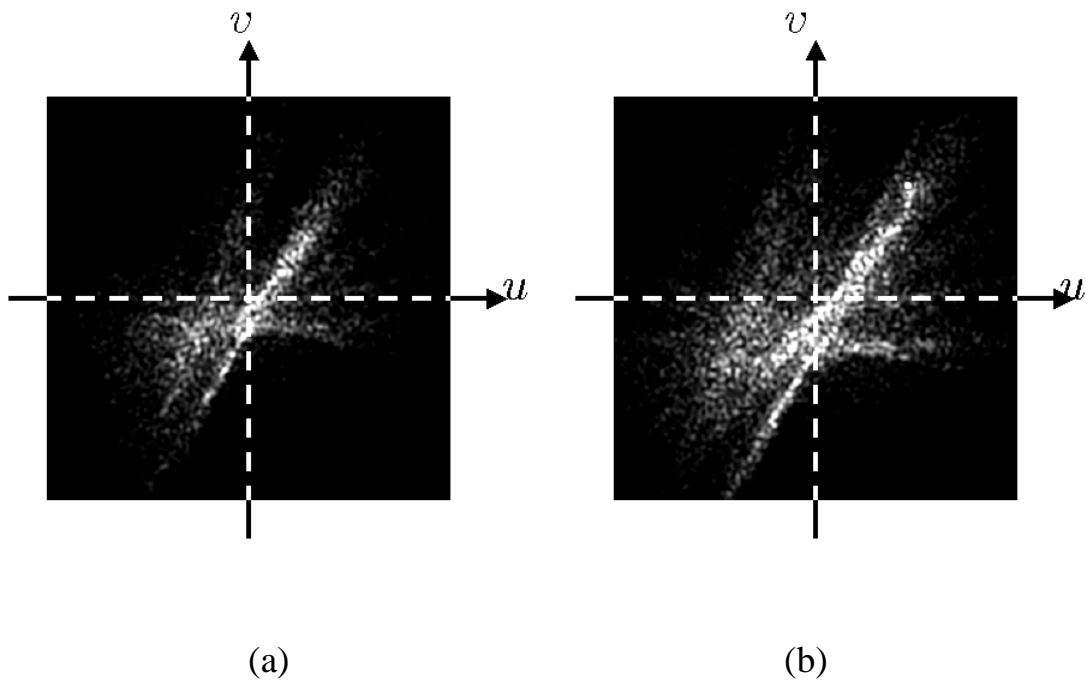


Fig. 7

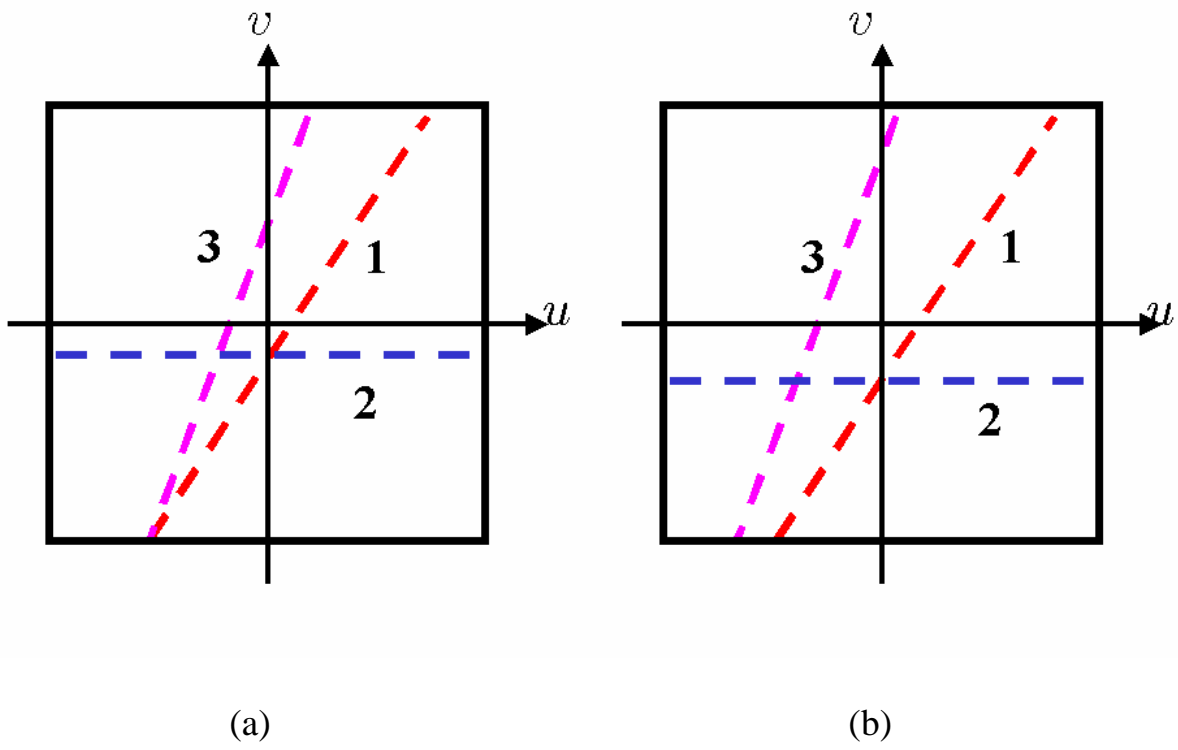


Fig. 8